Exp Fluids (2015) 56:80
DOI 10.1007/s00348-015-1946-2

RESEARCH ARTICLE

Influence of structural flexibility on the wake vortex pattern of airfoils undergoing harmonic pitch oscillation

B. Monnier[1] · A. M. Naguib[1] · M. M. Koochesfahani[1]

Received: 9 December 2014 / Revised: 17 March 2015 / Accepted: 18 March 2015

Abstract Reported herein is an investigation of the influence of the structural flexibility of sinusoidally pitching airfoils on the pattern of vorticity shed into the wake. For rigid airfoils, it is well known that, depending on the oscillation frequency and amplitude, this pattern takes the form of the classical or reverse von Kármán vortex street. The pattern may be characterized by the vortex circulation (Γ_o), vortex-to-vortex streamwise and cross-stream spacing (a and b, respectively), and vortex core radius (R). In the present work, these four parameters are obtained from particle image velocimetry measurements in the wake of airfoils consisting of a rigid "head" and flexible "tail" at chord Reynolds number of 2010 for different tail flexibilities. The results show that flexible airfoils exhibit the switch from classical to reverse von Kármán vortex street (i.e., change in the sign of b) at a reduced frequency of oscillation lower than their rigid counterpart. At a given oscillation frequency, the Strouhal number at which this switch occurs is smallest for a given airfoil structural flexibility; which becomes stiffer with increasing frequency. Using Strouhal number based on the *actual* trailing edge oscillation amplitude, reasonable scaling is found of the dependence of not only b but also Γ_o, a and R on the motion and structure parameters for all airfoils investigated. These results are complemented with analyses using a vortex array model, which together with the identified scaling of the wake vortex parameters, provide basis for the computation of the net thrust acting on the airfoil.

✉ A. M. Naguib
naguib@egr.msu.edu

[1] Michigan State University, East Lansing, MI 48104, USA

1 Introduction

Microair vehicles (MAVs), in low count or swarms, will likely become indispensable in the future in addressing a wide range of existing applications such as search and rescue operations, source identification/real-time tracking of spills of harmful substances into the atmosphere and reconnaissance missions. Normally, MAVs have small size and operate at low speed such that the associated Reynolds number is low (typically in the range: 10^3–10^5). Understanding of the aerodynamics at this low range of Reynolds numbers is lacking as traditional aerodynamics knowledge is based on high Reynolds number airfoils with thin attached boundary layers that operate under steady or quasi-steady conditions. Faced by the challenges of adequate lift generation in low Reynolds number flight based on traditional aerodynamics (Lissaman 1983; Mueller and DeLaurier 2003), and observation of nature's flying animals, a major departure in MAVs aerodynamics is the considerations of flapping wing designs where highly unsteady operating conditions are to be exploited instead of avoided (Koochesfahani 1989; Lai and Platzer 1999; Young and Lai 2004). Furthermore, efficient propulsion, high maneuverability and tolerance to wind gusts/flow disturbances are desirable traits that can be potentially attained with flapping wings. These advantages have prompted a surge in recent years in the study of flapping wing aerodynamics.

A canonical configuration that has received considerable interest in studying the fundamentals of flapping wing aerodynamics is that of periodically pitching and/or heaving airfoil (e.g., Koochesfahani 1989; Lai and Platzer 1999; Young and Lai 2004; Anderson et al. 1998; Ol 2007; Shyy et al. 2008). Experimental and computational investigations over a wide range of oscillation amplitudes, frequencies and phase lags (between the pitch and heave,

Published online: 03 April 2015

or plunge, motions) have all demonstrated that the airfoil wake is characterized by patterns of concentrated vorticity shed from the airfoil's trailing edge (TE) alone, or in combination with vorticity shed from the airfoil's leading edge. The wake vortex patterns and the forces developing on the airfoil are interdependent. For example, it is well known that the establishment of thrust force on a pitching or heaving airfoil is associated with the formation of the so-called reverse von Kármán street, where the position of positive- and negative-circulation vortices above/below the wake's centerline is opposite to the their position when the airfoil is not oscillating. Accompanying this change in the wake vortex pattern, which was first identified theoretically in Von Kármán and Burgers (1943), is a change in the mean velocity profile across the wake from one exhibiting momentum deficit to one associated with momentum excess (or jet-like) when drag and thrust are generated, respectively (Koochesfahani 1989). This switch from drag to thrust, however, does not coincide exactly with the point at which the mean velocity profile becomes jet-like because of additional drag associated with reduction in the wake pressure, which may be linked to the root-mean-square cross-stream velocity fluctuation (Bohl and Koochesfahani 2009).

The organization of shed vorticity into spatially localized distribution in the wake makes the latter amenable to simplified, structure-based modeling. Von Kármán's vortex street model (Von Kármán and Burgers 1943) of an array of inviscid point vortices superposed on uniform freestream velocity is a classical example of this type of modeling. Recently (Naguib et al. 2011), we extended von Kármán's ideas by replacing the inviscid point vortices with finite viscous-core counterparts. Employing a Gaussian vorticity distribution to represent the vortex core, we were successful in reproducing experimental measurements in the wake of a periodically pitching NACA 0012 airfoil with high accuracy (as exemplified in Fig. 1 for the case of a reverse Kármán street).

The objective of the present work was to examine the wake vortex pattern parameters b, Γ_o, a and R (as defined in the caption of Fig. 1) for harmonically pitching airfoils with different chord-wise structural flexibilities. First, the

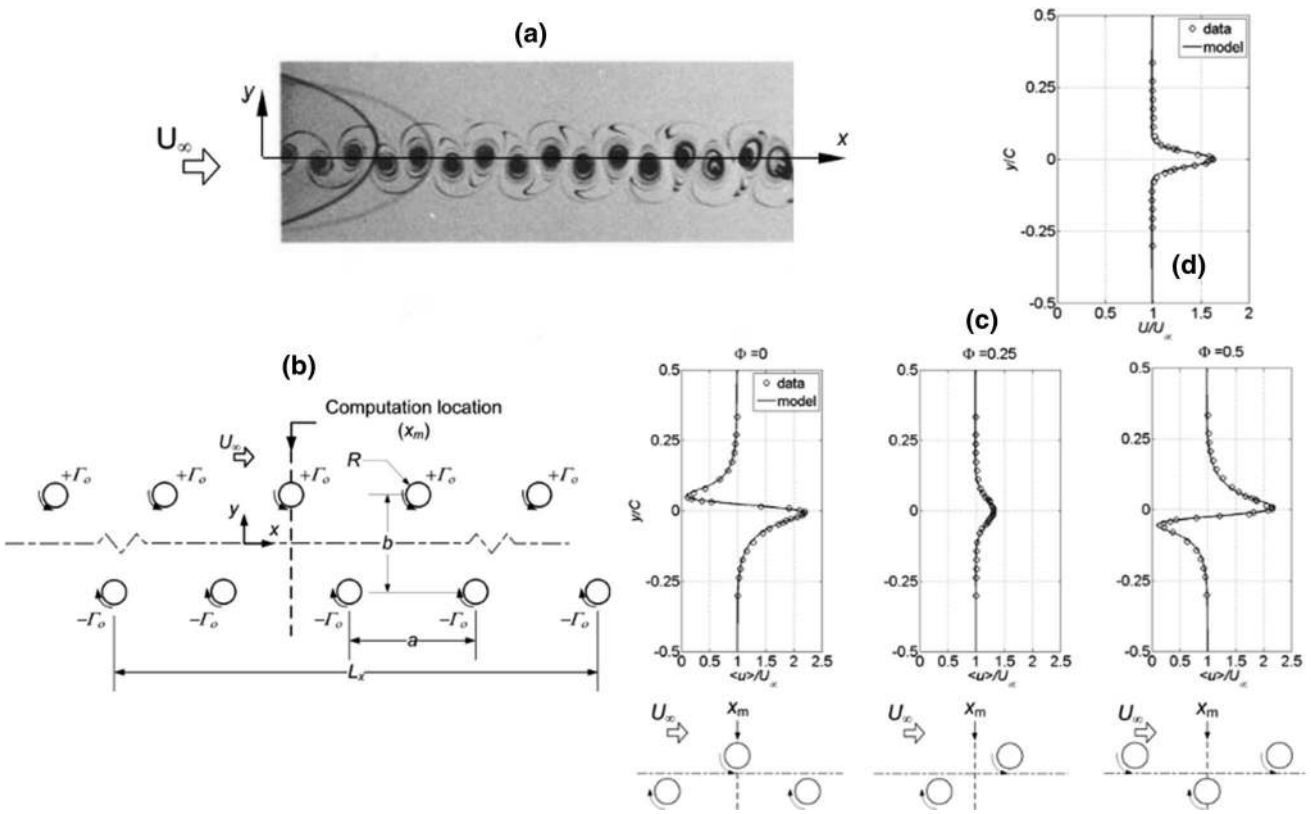

Fig. 1 **a** Flow visualization of the vortex structures in the wake of a harmonically oscillating NACA 0012 airfoil (Koochesfahani 1989); **b** frozen vortex array model (Naguib et al. 2011) of the wake vortex structure: a is the wavelength, b the cross-stream vortex spacing, Γ_o the vortex circulation, R the vortex core radius, U_∞ the freestream velocity and L_x the streamwise length spanned by the vortex array; **c** measured and predicted streamwise velocity profiles across the wake at one chord c downstream of the TE for different phases of the oscillation cycle (corresponding vortex locations relative to the calculation location are shown beneath the profiles); **d** measured (*symbols*) and predicted (*line*) profiles of the mean streamwise velocity, showing the jet-like profile characteristic of a reverse Kármán vortex street

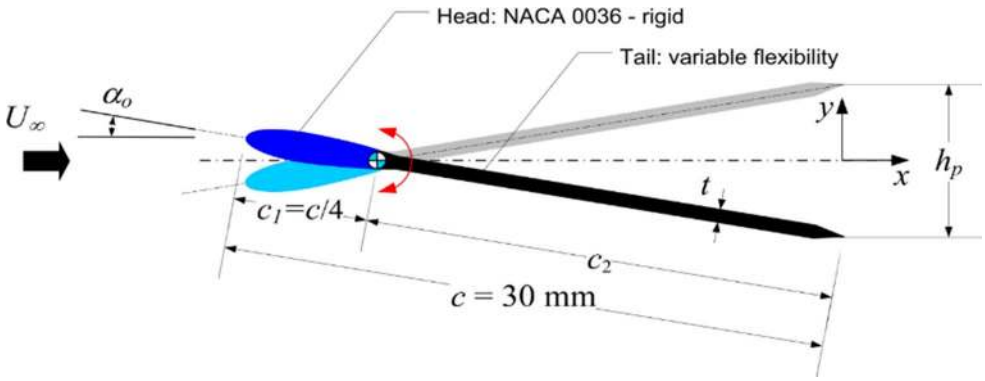

Fig. 2 Schematic of the airfoil geometry, coordinate system and relevant parameters. The origin of x coincides with the trailing edge of the rigid airfoil at zero angle of attack

general relationship between variation in these parameters and the mean thrust force acting on the airfoil will be investigated using the vortex array model of Naguib et al. (2011). Subsequently, the influence of airfoil flexibility and oscillation frequency and amplitude on the wake vortex parameters will be examined employing an experimental study. The combination of the model and the experimental results will help identify airfoil flexure characteristics and motion parameters that are favorable to thrust generation. This information may then be capitalized upon in future wake control schemes aiming to manipulate the thrust acting on the airfoil via alteration of the wake vortex configuration.

It should be noted that though several studies exist of airfoils having chord-wise structural flexibility [e.g., (Heathcote and Gursul 2007; Liu 2009; Thiria and Godoy-Diana 2010; Kang et al. 2011)], none of these is focused on quantifying the wake vortex pattern and their dependence on motion and structural parameters. Instead, these studies, and others not cited here for brevity, are concerned with the effect of structural flexibility on the forces and thrust efficiency. In addition to enabling new ideas for wake control, as stated above, the present focus on the wake vortex pattern is motivated by the possibility of coupling knowledge of the wake pattern parameters with the vortex array model in a semiempirical tool for engineering calculations of the net thrust acting on oscillating airfoils. Specifically, we seek to identify appropriate scaling of the vortex pattern parameters with variation in the airfoil's motion and structural parameters. Such empirically identified scaling can then be used to specify the vortex configuration for a given application, which in turn can be used with the vortex array model to calculate the thrust force.

2 Experimental setup

The present measurements take place in a free-surface closed-return water tunnel with test section dimensions of 19 cm × 15.3 cm × 43.4 cm in height, width and length, respectively. The geometry of the airfoil employed is depicted in Fig. 2. The airfoil consists of a rigid "head" portion that has a NACA 0036 profile, and a "tail" piece that is made from either a rigid or a flexible material. The chord of the airfoil is $c = 30$ mm, with the head stretching over 7.5 mm length. The airfoil's thickness ratio based on c is 0.09. The airfoil is centered along the width of the test section while stretching from just above the bottom wall to just below the free surface, with <2 % of span clearance on either end. The corresponding aspect ratio is 4.23. No significant surface waves are found at the airfoil motion settings reported here.

When using a flexible material, the thickness t of the tail part is varied to change the flexibility of the airfoil. The non-dimensional parameter G_1 (also frequently denoted by π_1 in the literature) is used to characterize the structure flexibility; it is defined as:

$$G_1 = \frac{Et^3/(12(1-\nu^2))}{\rho U_\infty^2 c_2^3}, \tag{1}$$

where E and ν are Young's modulus and Poisson's ratio for the tail material, respectively, ρ is the fluid density, U_∞ is the freestream velocity, and c_2 is the length of the tail (22.5 mm). For all experiments, the airfoil is pitched around the ¼ chord point (at the junction of the head and tail) and the freestream velocity is nominally set to 6.7 cm/s (corresponding to a chord Reynolds number $Re_c = 2010$).

Two designs of the airfoil are used. In the initial design, the rigid part of the airfoil is obtained via standard rapid prototyping and the tail is a rectangular piece of silicone rubber that is fitted in a slot in the downstream end of the head. This initial design is used in preliminary experiments employing hydrogen (H_2) bubbles to visualize the wake. In the second design, the entire airfoil is fabricated using a Connex350 3D printer which is capable of printing objects using two materials, resulting in seamless integration of the head and tail. The second design is used in experiments where particle image velocimetry (PIV) is employed to obtain detailed measurements of the velocity in the wake

Table 1 Experimental conditions

	Flow visualization/initial airfoil design	PIV/new design
Frequency f	1–5 Hz in increments of 1 Hz	3.29, 4.27 and 5.23 Hz
Amplitude α_o	1°–10° in increments of 1°	2°–7° in increments of 1°
Reduced frequency $k = \pi fc/U_\infty$	1.41–7.03	4.63, 6.19 and 7.35
Strouhal number $St = fh_p/U_\infty$	0.01–0.58	0.08–0.43
t (mm)	0.8 and 1.6	0.8, 1.0 and 1.6
G_1	0.6, 4.5 and 97 (rigid)	0.7, 1.3, 5.3 and 97 (rigid)

of the airfoil. The characteristics (t and G_1) of both designs are shown in Table 1 for all the experiments presented here.

In both the flow visualization and PIV studies, the airfoil is pitched symmetrically around a mean angle of attack of zero with an amplitude α_o and frequency f. Table 1 summarizes the range of frequencies and amplitudes investigated in this work. The corresponding reduced frequencies and Strouhal numbers are also listed; note that h_p is the peak-to-peak trailing edge displacement amplitude of the rigid airfoil; see Fig. 2. The airfoil pitching motion is imposed using a servo motor controlled by a Galil DMC-1030 controller. The motor is installed on top of the test section, and the airfoil is held vertically. The angular motion of the motor is captured using an optical encoder.

The H_2 bubble flow visualization is performed using a 50-μm (0.002-in.)-diameter stainless steel wire that is placed just downstream of the trailing edge of the airfoil. A function generator delivering a square wave signal, amplified by a dedicated amplifier, provides the voltage necessary to activate the H_2 electrolysis. The frequency of the square wave is set to 15 Hz, and the resulting hydrogen-bubble images are recorded at a rate of 30 frames/s using a Pulnix 1040 camera (1024 pixel × 1024 pixel).

For PIV measurements, silver-coated hollow glass spheres (Potter Industries Inc.-SH400S20) with a mean diameter of about 20 μm are used to seed the flow. A 500 mW Lasiris Magnum SP Laser operating at a wavelength of 680 nm is employed to illuminate the glass spheres in the wake of the airfoil at about mid-span. A 12-bit 1392 pixel × 1024 pixel PCO Pixelfly QE camera is used to record the PIV snapshots. The camera and laser pulses are synchronized using a Stanford Research Systems DG535 digital delay generator. One thousand pairs of images are acquired and processed for each case at the maximal frequency allowed by our setup (5 Hz). The PIV region of interest is limited to the wake region and is about 1.5 chord long in the streamwise (x) direction and 2 chord wide in the cross-stream (y) direction. Interrogation of PIV images is done using the code by Thielicke and Stamhuis (http://pivlab.blogspot.com), yielding a velocity vector for every 16 pixel × 16 pixel interrogation region (corresponding to $0.028c \times 0.028c$). A three-point estimator with Gaussian fit is used to determine the cross-correlation peak, which yields a 0.1 pixel *rms* uncertainty in particle displacement (Raffel et al. 2007) or 0.11 cm/s uncertainty in the velocity. Vector validation is implemented using a standard deviation and a local median check. The percentage of bad vectors is typically 2–5 %. These are replaced via interpolation.

The *actual* trailing edge peak-to-peak displacement ($h_{p,actual}$) is determined from images of the trailing edge, which is captured in the field of view of the flow visualization and PIV pictures. The trailing edge position is found as function of time, and the resulting time series is phase-sorted based on the imposed frequency of oscillation. The phase-sorted signal is checked for symmetry and harmonic fidelity, and only cases exhibiting asymmetry of <5 % of the peak-to-peak of the signal and harmonic fidelity of better than 99 % are presented in the current paper. Only a handful cases, particularly at the highest frequency and thinnest airfoil tail, did not meet these criteria. For all other cases, $h_{p,actual}$ is determined as the difference between the maximum and minimum of the phase-sorted signal. The uncertainty in measuring the trailing edge displacement is estimated as the root-mean-square of the difference between the measured and expected displacement of the rigid airfoil for all amplitudes and frequencies.

3 Model description and implications

In the following, the relationship between the wake vortex parameters, b, Γ_o and a and the mean thrust acting on the airfoil is explored using the vortex array model demonstrated in Fig. 1. The focus of the analysis is on "simple" wakes that are characterized by shedding of one positive and one negative vortex per airfoil oscillation cycle. Also, only the reverse Kármán vortex street configuration is considered, where the vortex with positive (ccw) circulation is above the wake's centerline (in the present choice of coordinate system), and vice versa, and the mean velocity profile is jet-like. This is done to focus the analysis on wake vortex characteristics that are favorable for thrust generation. The analysis does include the "neutral wake," where the centers of the opposite-signed vortices are colocated on the wake centerline, as a limiting case that separates

conditions leading to mean velocity deficit from those leading to mean velocity excess in the wake and the possibility of producing net mean thrust on the airfoil. Furthermore, to get insight into the influence of each of the three wake vortex parameters on the mean thrust, each parameter is varied independently from the other two. Inevitably, this approach results in a combination of parameters that may not coexist in physical observations since in reality all three parameters cannot be varied independently by changing the oscillation parameters of the airfoil. Nevertheless, the explored parameter space does include parameter combinations that *are* physically observable. Moreover, from flow control perspective, information from the explored parameter space can be useful for devising a wake control scheme that produces a combination of wake vortex parameters desirable for thrust generation yet inaccessible through the oscillation of the airfoil alone.

In Naguib et al. (2011), we showed that the mean streamwise force coefficient (C_f) acting on a harmonically pitching airfoil computed using the vortex array model is in good agreement with published results. For reference, the specific equations of the model are given by:

$$u(x,y) = U_\infty - \sum_{i=1}^{N} \frac{\Gamma_i(r_i)}{2\pi} \frac{(y-y_{ci})}{r_i^2} \tag{2}$$

$$v(x,y) = \sum_{i=1}^{N} \frac{\Gamma_i(r_i)}{2\pi} \frac{(x-x_{ci})}{r_i^2} \tag{3}$$

with

$$\Gamma_i(r_i) = \Gamma_o \left[1 - e^{-(r_i/R_i)^2}\right], \tag{4}$$

where subscript i represents the ith vortex in an array of N vortices (half of which have positive (ccw) circulation and the other half have negative (cw) circulation), x_c and y_c indicate the coordinates of the vortex core center, r is the distance from the core center to point (x, y) where the streamwise and cross-stream velocity components, u and v, respectively, are computed, and the remainder of the symbols are defined in the caption of Fig. 1.

To calculate the mean streamwise force coefficient C_f, the computed mean and root-mean-square (*rms*) velocity profiles at a given streamwise location in the wake are substituted in the streamwise integral momentum equation, which simplifies to the following form for the flow considered [see (Bohl and Koochesfahani 2009; Naguib et al. 2011)]:

$$C_f = \frac{2}{c} \int_{-\infty}^{\infty} \left[\frac{U}{U_\infty} \left(\frac{U}{U_\infty} - 1 \right) + \frac{u_{rms}^2}{U_\infty^2} - \frac{v_{rms}^2}{U_\infty^2} \right] \mathrm{d}y, \tag{5}$$

where U is the mean streamwise velocity, u_{rms} and v_{rms} are the streamwise and cross-stream *rms* velocities, respectively. Equation (5) yields a positive value for C_f when a net thrust is acting on the airfoil and a negative value in the case of net drag. At sufficiently high oscillation frequency and/or amplitude, the wake structure switches to the reverse von Kármán configuration and the term on the right-hand side involving the mean streamwise velocity becomes positive, and hence, together with the term involving the *rms* of the same velocity component, contributes to thrust. On the other hand, the term involving v_{rms} is negative definite and hence accounts for the presence of a drag component in C_f. In fact, this term is a substitution for the mean pressure term at the x location of the analysis, using the cross-stream integral momentum equation. For convenience, upon establishment of the reverse von Kármán wake, C_f may be decomposed into thrust and drag components ($C_{f,t}$ and $C_{f,d}$, respectively), where:

$$C_{f,t} = \frac{2}{c} \int_{-\infty}^{\infty} \left[\frac{U}{U_\infty} \left(\frac{U}{U_\infty} - 1 \right) + \frac{u_{rms}^2}{U_\infty^2} \right] \mathrm{d}y \tag{6}$$

$$C_{f,d} = -\frac{2}{c} \int_{-\infty}^{\infty} \left[\frac{v_{rms}^2}{U_\infty^2} \right] \mathrm{d}y \tag{7}$$

In the following discussion of each vortex parameter, the dependence of the model-computed profiles of U, u_{rms} and v_{rms} on each of the wake vortex parameters will be examined first. The outcome of this examination will be subsequently used to interpret the trend seen in C_f variation with the wake vortex parameter under consideration. The range of parameter values employed in the analysis encompasses the values observed in the experimental component of the present investigation while spanning a somewhat wider parameter space to reveal some interesting limits of the wake configuration.

3.1 Implication of cross-flow vortex spacing (b)

The cross-flow vortex spacing b is defined as the y-coordinate of the positive-signed vortex minus that of the negative-signed vortex. As mentioned above, the analysis is conducted for the neutral and reverse von Kármán wakes, corresponding to $b/c \geq 0$. Figure 3 (left) shows the predicted mean streamwise velocity profiles for different values of b/c. As expected, for the neutral wake ($b/c = 0$), the velocity profile is uniform and has a magnitude equal to the freestream velocity. As b/c increases, the profile becomes jet-like with the peak velocity exceeding the freestream velocity and becoming progressively larger. Beyond $b/c = 0.1$, the peak velocity magnitude does not increase anymore and additional increase of b/c merely results in the profile becoming wider in the y direction. Moreover, the shape of the profile becomes top-hat-like, reminiscent

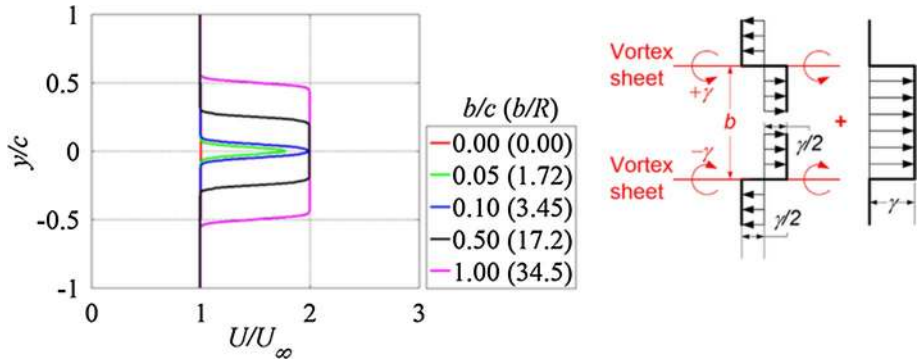

Fig. 3 Mean streamwise velocity profiles computed using the vortex array model for different values of b/c and $\Gamma_o/cU_\infty = 0.4$, $a/c = 0.4$ and $R/c = 0.029$ (*left*). Profile of the velocity induced by two opposite-signed vortex sheets (*right*). γ is the circulation per unit length

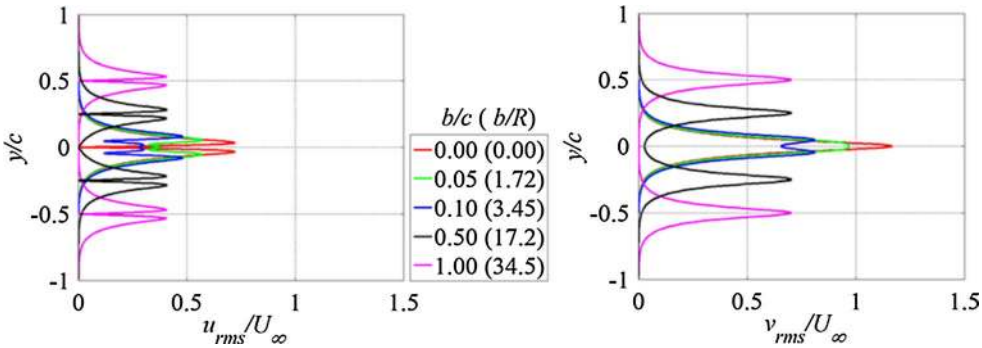

Fig. 4 Cross-stream profiles of the *rms* streamwise (*left*) and cross-stream (*right*) velocity computed using the vortex array model for different values of b/c and $\Gamma_o/cU_\infty = 0.4$, $a/c = 0.4$ and $R/c = 0.029$

of that associated with the presence of two opposite-signed infinite vortex sheets (Fig. 3, right). In the latter case, the velocity jump across the vortex sheet is given by γ (where γ is the circulation per unit length). Interestingly, for $b/c > 0.1$, the velocity jump computed from the vortex array model is found to be equal to the vortex circulation divided by the wavelength: Γ_o/a. Hence, it is expected that as $b/c \to \infty$, the wake vortex pattern may be modeled by two opposite-signed vortex sheets with $\gamma = \Gamma_o/a$. In this "vortex-sheet limit" (*vsl*), the resulting mean thrust coefficient could be easily computed using the momentum integral equation, yielding:

$$C_{f,vsl} = 2\left(\frac{\gamma}{U_\infty} + 1\right)\frac{\gamma}{U_\infty}\frac{b}{c} = 2\left(\frac{\Gamma_o}{aU_\infty} + 1\right)\frac{\Gamma_o}{aU_\infty}\frac{b}{c} \quad (8)$$

Equation (8) is exact for an idealized, zero thickness, vortex sheet, where the velocity jump in the top-hat profile is abrupt. In the vortex array model, and in the actual flow, the vortices have finite viscous core which results in less abrupt change from the high to low velocity in the top-hat profile (Fig. 3, left). The "degree of abruptness" of this transition will depend on the viscous-core radius R. Similarly, the value of b/c at which the profile transitions from being bell-shaped to being top-hat-like ($b/c \approx 0.1$ in Fig. 3, left) will also depend on the value of R.

Referring to Fig. 3, up to the point where the U profile becomes top-hat-like, the increase in b/c increases *both* the overall level of the velocity and the cross-stream breadth of the profile. Both of these factors contribute to the increase in thrust with increasing b/c [through the first term on the RHS of Eq. (6)]. Once the velocity profile becomes top-hat like, further increase in b/c is only associated with increase in the width of the domain of nonzero ($U/U_\infty - 1$), which should lead to linear variation of C_f with b/c, provided that the C_f terms related to u_{rms} and v_{rms} also vary linearly with b/c, or remain invariant. Indeed, for sufficiently large values of b/c, both of these terms become constant as implied from the plot of the u_{rms} and v_{rms} cross-stream profiles in Fig. 4. In particular, for b/c of roughly 0.5 (a value that should also depend on R in the same way the b value at which the velocity profile becomes top-hat-like also depends on R) or higher, the area under the u_{rms} and v_{rms} profiles (and correspondingly under u_{rms}^2 and v_{rms}^2) remains invariant. Therefore, C_f is expected to vary linearly with b/c at large values of b/c, which is consistent with the results displayed in Fig. 5. Figure 5 also demonstrates that the larger b/c is, the larger the thrust, and that the vortex-sheet limit provides, at least, good qualitative description of the relationship between C_f and b.

3.2 Implication of vortex circulation (Γ_o)

The cross-stream profiles of U/U_∞, u_{rms}/U_∞ and v_{rms}/U_∞ for different values of Γ_o/cU_∞ are given in Figs. 6 and 7. The magnitude of all three velocities increases with circulation,

as would be expected from inspection of Eqs. (2) and (3). In fact, the latter equations show that the dependence on Γ_o is linear, which implies that the profiles can be made to collapse by scaling them with a velocity scale based on Γ_o. Choosing the velocity scale to be Γ_o/a (also the circulation per wavelength; the choice of a instead of c for the length scale will be justified below), the profiles may be given by the invariant forms (when a, b and R are fixed):

$$\begin{aligned}\frac{(U-U_\infty)}{\Gamma_o/a} &= f_U\left(\frac{y}{c}\right)\\ \frac{u_{rms}}{\Gamma_o/a} &= f_u\left(\frac{y}{c}\right)\\ \frac{v_{rms}}{\Gamma_o/a} &= f_v\left(\frac{y}{c}\right)\end{aligned} \tag{9}$$

Substituting these expressions in Eq. (5) yields:

$$C_f = 2\left(A\frac{\Gamma_o}{aU_\infty}+B\right)\frac{\Gamma_o}{aU_\infty} \tag{10}$$

with

$$A = \int_{-\infty}^{\infty}\left(f_U^2\left(\frac{y}{c}\right)+f_u^2\left(\frac{y}{c}\right)-f_v^2\left(\frac{y}{c}\right)\right)\mathrm{d}\frac{y}{c} \tag{11}$$

$$B = \int_{-\infty}^{\infty} f_U\left(\frac{y}{c}\right)\mathrm{d}\frac{y}{c} \tag{12}$$

Referring to the right-hand side of the equations set (9), in the idealized vortex-sheet limit, f_u and $f_v \to 0$, and f_U becomes top-hat with a value of one for $-b/c \le y/c \le b/c$, and zero otherwise, reducing Eq. (8) to (10). In this limit, both A and B are positive and C_f increases monotonically with Γ_o. More generally, A may be positive or negative. The $f_u^2 - f_v^2$ term is generally negative, as discussed in connection with Fig. 4, so the sign of A depends on the balance of f_U^2 and $f_u^2 - f_v^2$ terms. In most instances, the former term dominates, but, as will be seen in section below, at sufficiently long wavelength a the change in the profile shape f_v is such that it is the dominant term in the integrand in Eq. (11), leading to a negative A value, and non-monotonic variation in C_f with Γ_o. The difference in the character of C_f variation with Γ_o between short and long wavelength can be seen in Fig. 8, where C_f is plotted versus Γ_o/cU_∞ for the same cases considered in Figs. 6 and 7. The right plot in Fig. 8 provides a magnified view for the two cases with the longest wavelengths to reveal the aforementioned non-monotonic behavior. For these two cases, at low values of

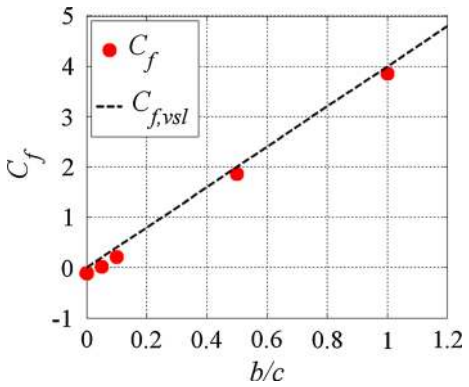

Fig. 5 Variation of the mean streamwise force coefficient with the cross-stream vortex spacing, obtained using the vortex array model for different values of b/c and $\Gamma_o/cU_\infty = 0.4$, $a/c = 0.4$ and $R/c = 0.029$. The *broken line* represents the vortex-sheet limit

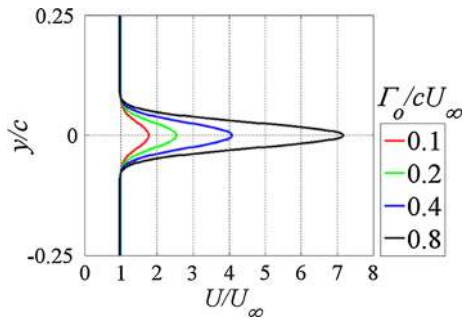

Fig. 6 Mean streamwise velocity profiles computed using the vortex array model for different values of Γ_o/cU_∞ and $a/c = 0.1$, $b/c = 0.05$ and $R/c = 0.029$

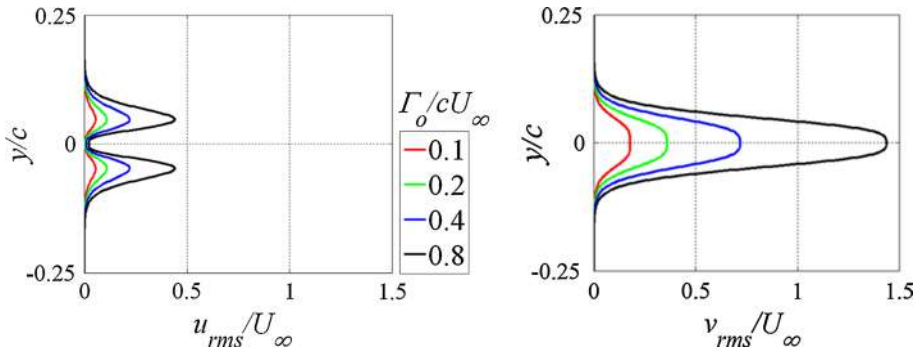

Fig. 7 Root-mean-square profiles computed using the vortex array model for different values of Γ_o/cU_∞ and $a/c = 0.1$, $b/c = 0.05$ and $R/c = 0.029$: streamwise (*left*) and cross-stream (*right*) velocity

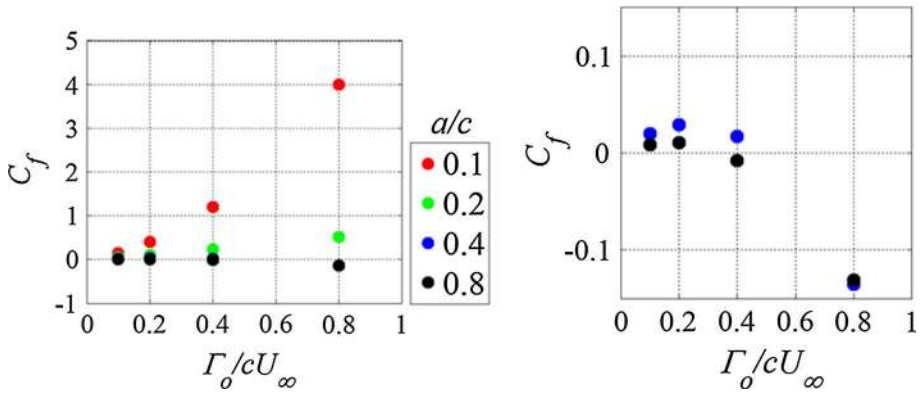

Fig. 8 Variation of C_f with circulation (*left*) computed using the vortex array model for different values of a/c and $b/c = 0.05$ and $R/c = 0.029$. Magnified view of the results for $a/c = 0.4$ and 0.8 (*right*)

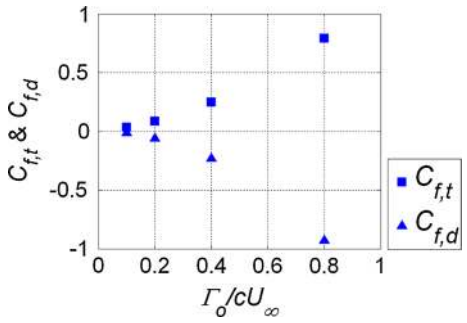

Fig. 9 Variation of the thrust and drag components of C_f with circulation computed using the vortex array model for $a/c = 0.4$, $b/c = 0.05$ and $R/c = 0.029$

circulation, C_f increases with increasing circulation as the linear term Γ_o/aU_∞ in Eq. (10) (with positive constant B) is initially larger than the quadratic term (with negative constant A). With additional increase in circulation, eventually, the quadratic term becomes larger and C_f decreases with increasing circulation, even becoming negative. Under these conditions, essentially the increase in circulation results in the pressure drag increasing with circulation at a faster rate than the thrust. This is illustrated in Fig. 9, where the thrust and drag components of C_f [see Eqs. (6) and (7), respectively] are plotted versus Γ_o/cU_∞ for $a = 0.4$.

3.3 Implication of wavelength (a)

Figure 10 depicts mean velocity profiles obtained for different values of a/c, while other parameters are kept constant. The left plot in the figure displays the mean velocity normalized by the freestream velocity, and the right plot shows the mean velocity *excess*, above the freestream velocity, normalized by Γ_o/a. When normalized by U_∞, U decreases with increasing wavelength. The decrease in the mean velocity excess is inversely proportional to a, given that the profiles of the velocity excess for different values of a/c collapse on a common curve when normalized by Γ_o/a. This shows that the form $(U - U_\infty)a/\Gamma_o = f_U(y/c)$ is invariant for variation in a and Γ_o and that Γ_o/a is an appropriate scale for the mean velocity excess. In contrast, no appropriate scaling with variation of a can be found for the *rms* velocity profiles. In particular, referring to Fig. 11 where the profiles are displayed, the profiles exhibit non-monotonic variation (as can be seen, for example, at $y/c = 0$), or even change shape (see the u_{rms} profile shape changing from "double- to triple-peaked") with increasing a.

The decrease of U with increasing a causes the overall magnitude and cross-stream breadth of $(U - U_\infty)/U_\infty$ profile to become less than that of the v_{rms}/U_∞ profile at long wavelength, as can be seen, for example, by comparing the profiles at $a = 0.8$ (black line) in Figs. 10 and 11. Thus, the v_{rms} term in Eq. (5) can become sufficiently dominant such that a net drag rather than thrust is produced on the airfoil. This is consistent with the earlier discussion regarding the different qualitative behavior of C_f with circulation at short versus long wavelength. Overall, the variation of the velocity profiles shown in Figs. 10 and 11 suggests that C_f decreases with increasing wavelength. This is confirmed from computation of the corresponding C_f variation with a/c, shown in Fig. 12. It is noteworthy that, to leading order, a/c is inversely proportional to k; thus, the reduction of C_f with increasing a/c is consistent with the known decrease in C_f with decreasing reduced frequency, including, ultimately, the transition from thrust to drag at sufficiently low frequencies.

4 Experimental results

With the insight gained from the above analysis concerning the relationship between C_f and the different wake vortex parameters, the dependence of these parameters on the airfoil flexibility and motion parameters is now examined. The observed wake flow in the majority of the cases investigated using PIV is of the "simple" wake type that is characterized by shedding of one positive and one negative

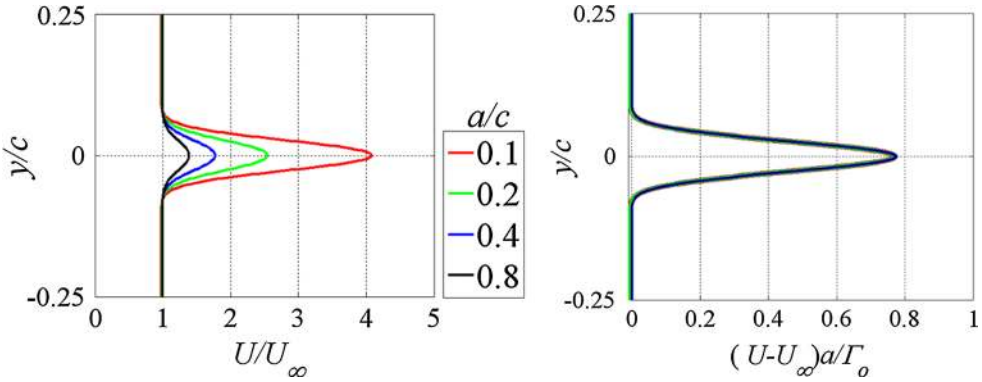

Fig. 10 Mean streamwise velocity profiles computed using the vortex array model for different values of a/c and $b/c = 0.05$, $\Gamma_o/cU_\infty = 0.4$ and $R/c = 0.029$ (*left*). The same profiles after subtracting the freestream velocity and normalizing by the circulation per wavelength are shown in the *right plot*

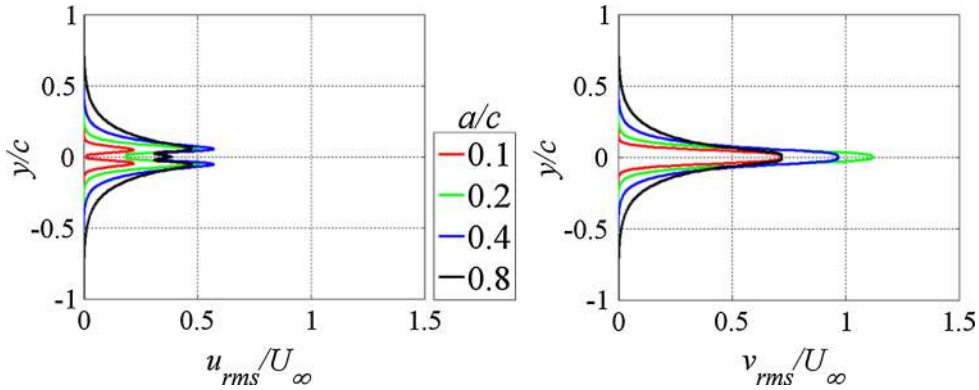

Fig. 11 Root-mean-square profiles of the streamwise (*left*) and cross-stream (*right*) velocity computed using the vortex array model for different values of a/c and $b/c = 0.05$, $\Gamma_o/cU_\infty = 0.4$ and $R/c = 0.029$

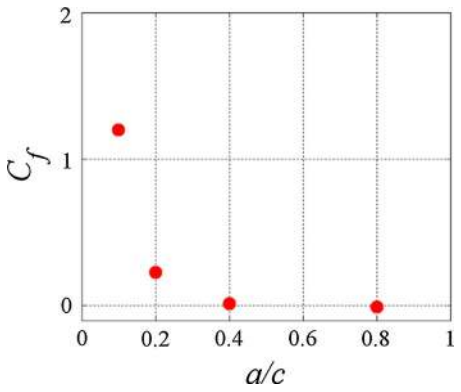

Fig. 12 Variation of Cf with wavelength computed using the vortex array model for different values of a/c and $b/c = 0.05$, $\Gamma_o/cU_\infty = 0.4$ and $R/c = 0.029$

vortex per airfoil oscillation cycle. Examples of such wakes are depicted using a snapshot of the phase-averaged vorticity for the rigid airfoil in Fig. 13, where the vortex pattern corresponds to classical, neutral and reverse von Kármán street. However, in some of the cases investigated, deviations from the simple wake pattern are found. These deviations manifest themselves in three typical forms: (1) wakes where the separating shear layer at the TE has not rolled up completely into a vortex (Fig. 14, left); (2) wakes with more than one vortex of the same sign are shed per oscillation cycle (Fig. 14 middle and right); (3) "deflected" wakes where the vortex trajectory is inclined to the streamwise direction (Fig. 14 right). These cases are excluded from the analysis conducted in the current work since it is difficult to extract the vortex characteristics in an unambiguous way.

4.1 Cross-flow vortex spacing (b)

Figure 15 depicts three wake visualization images organized in order of increasing airfoil flexibility (from left to right). In all three cases, the oscillation parameters are kept the same: $\alpha_o = 4°$, $k = 2.79$, $St = 0.09$. As seen from the figure, for the rigid airfoil, vortices with counter-clockwise (positive)/clockwise (negative) sense of rotation are observed on the left/right of the wake centerline (marked by the solid red line). This arrangement is similar to the natural wake of the airfoil (i.e., in the absence of the imposed oscillation), representing the conventional Kármán street, which is associated with mean velocity deficit in the wake. As the flexibility is increased by reducing G_1 to 4.5, the cross-stream spacing of the vortices b becomes smaller. Further decrease of G_1 to 0.6 causes the center of the vortex cores to become aligned with the wake centerline; i.e., $b = 0$, producing a neutral wake. This suggests that

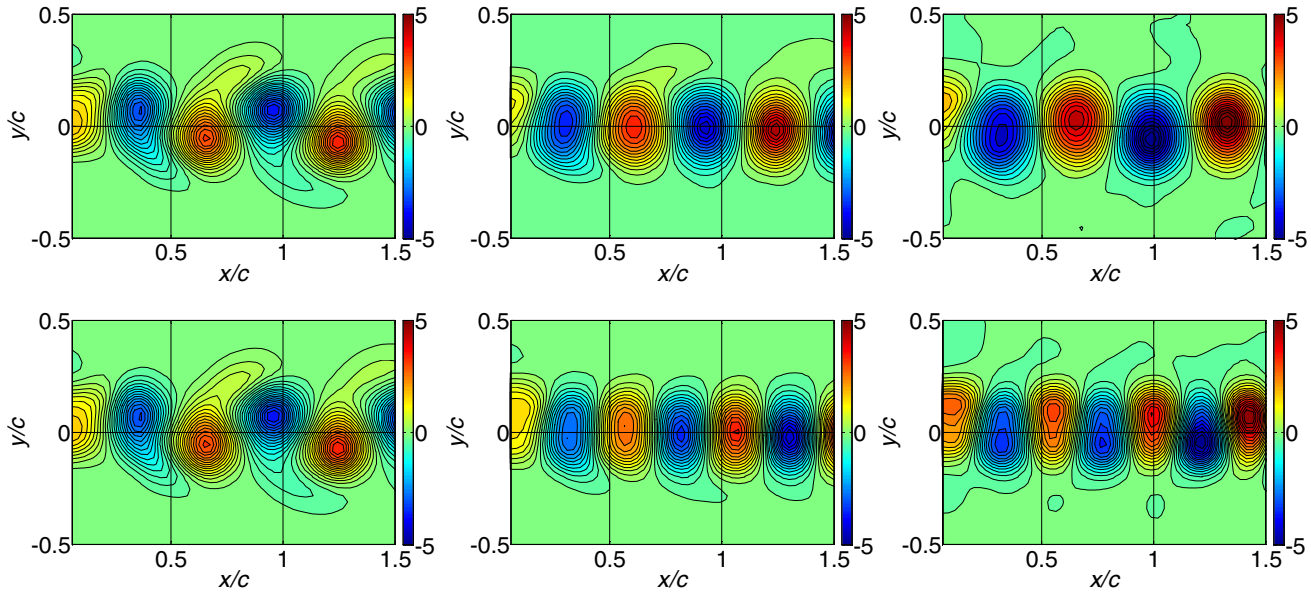

Fig. 13 Vorticity field snapshots for the rigid airfoil. *Top row* depicts cases corresponding to fixed oscillation frequency ($k = 4.63$) but different pitch angle amplitudes of 3° (*left*), 4° (*middle*) and 5° (*right*). *Bottom row* displays plots corresponding to fixed oscillation amplitude (3°) but different oscillation frequencies of $k = 4.63$ (*left*), 6.19 (*middle*) and 7.35 (*right*). The *color bar* indicates the vorticity value normalized by the chord length and freestream velocity: $\omega_z c/U_\infty$

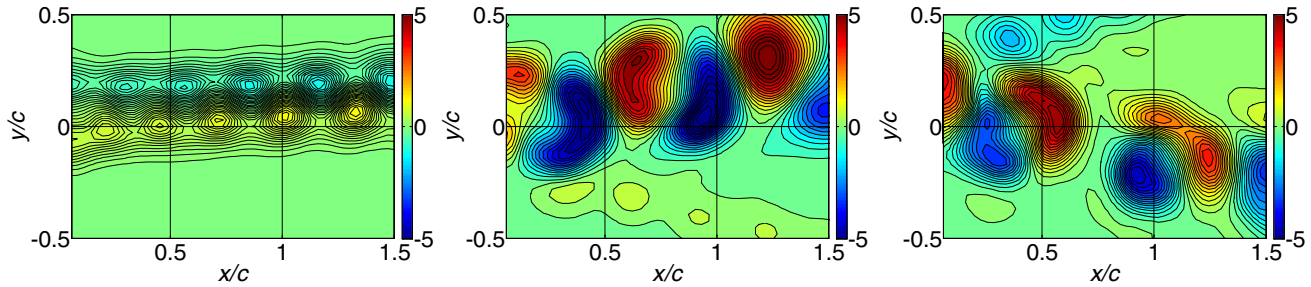

Fig. 14 Vorticity field snapshots demonstrating non-simple wake vortex patterns at $k = 7.35$: incomplete shear-layer roll-up for airfoil with $G_1 = 0.7$ (*left*), multiple same-sign vortices per oscillation cycle for rigid ($G_1 = 97$) airfoil (*middle*), and deflected wake and multiple same-sign vortices per cycle for airfoil with $G_1 = 5.3$ (*right*). The *color bar* indicates the vorticity value normalized by the chord length and freestream velocity: $\omega_z c/U_\infty$

the increased airfoil flexibility results in reduction in the net drag force acting on the airfoil for the specific airfoil motion parameters associated with the results in Fig. 15.

To test the above conclusion over a wide range of motion parameters, b is extracted from the flow visualization images at $x/c = 0.5$ over a range of oscillation amplitudes and frequencies. To achieve this, the center of each of the positive- and negative-signed vortices is visually identified as the center of the circular hydrogen-bubble pattern when it coincides with $x/c = 0.5$. The results are summarized in Fig. 16 where b/c is plotted versus the Strouhal number for three values of the reduced frequency. Since k was varied solely via changing the frequency, the results for a given k value essentially show the dependence of b on the oscillation amplitude for different airfoil flexibilities. It should be noted that negative b values correspond to the conventional von Kármán wake (with wake-like mean velocity profile), whereas positive values represent the reverse von Kármán street (with jet-like mean velocity profile in the wake). Overall, the results in Fig. 16 show that b/c increases with increasing oscillation amplitude and switches sign from negative to positive, reflecting the change in the streamwise force from drag to thrust. However, the switch from drag to thrust actually happens at a b value that is larger than zero due to the drag force associated with v_{rms} (Bohl and Koochesfahani 2009).

More significantly, the results show clear dependence on the wing flexibility. For all three k values considered, the flexible airfoils undergo the switch from drag to thrust at lower St value than the rigid airfoil. At the low reduced

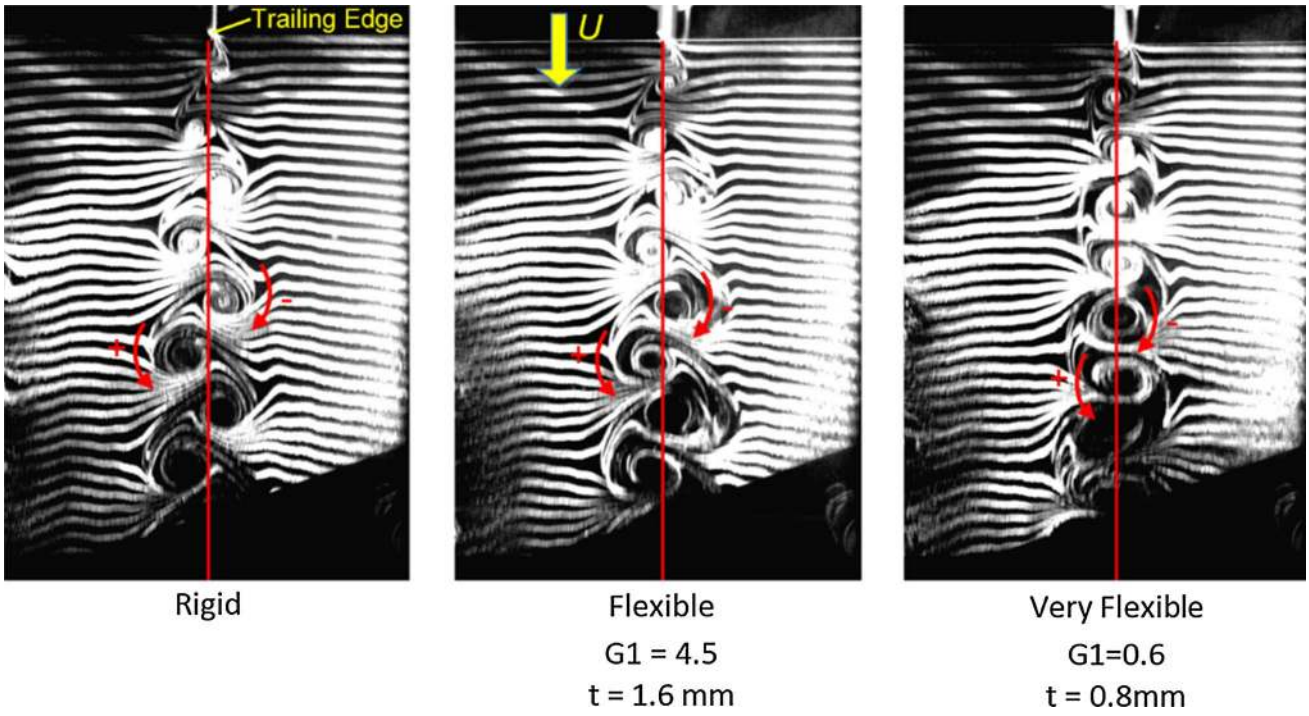

Fig. 15 Hydrogen-bubble flow visualization of the wake of the rigid (*left*) and flexible airfoils (*middle* and *right*) for $\alpha_o = 4°$, $k = 2.8$ and $St = 0.09$. The *red line* marks the wake centerline ($y = 0$)

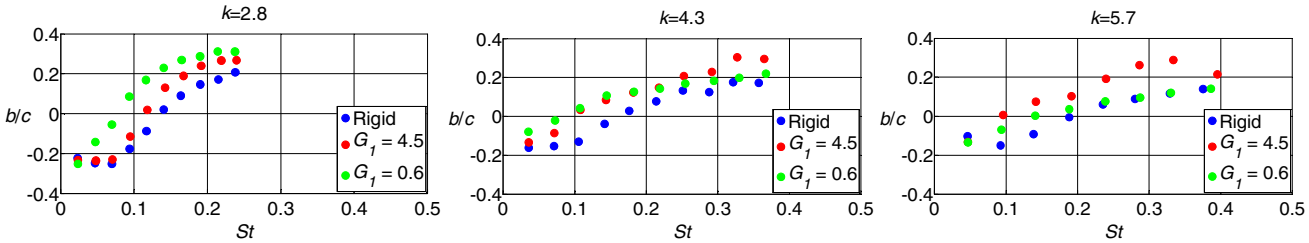

Fig. 16 Dependence of the cross-stream vortex spacing, determined from flow visualization, on the Strouhal number for different reduced frequency values: $k = 2.8$ (*left*), 4.3 (*middle*) and 5.7 (*right*)

frequency ($k = 2.8$), the most flexible airfoil exhibits this switch at *St* value lower than that of the intermediate flexibility one, while the latter undergoes this change at *St* value lower than that of the rigid airfoil. As the reduced frequency increases, the *St* value at which the intermediate-flexibility airfoil exhibits the switch in wake structure becomes progressively smaller, equaling that of the most flexible airfoil at $k = 4.3$, and becoming the smallest of all airfoils at $k = 5.7$. These results suggest that at a given reduced frequency, there is an optimum airfoil flexibility which produces thrust at the smallest amplitude of oscillation. The presence of such optimal flexibility in relation to the thrust coefficient was also identified in Heathcote and Gursul (2007). Specifically, using airfoils with similar geometry to that used here but undergoing heaving motion at substantially larger Re_c (in the range 9000–27,000), an optimum airfoil flexibility was found to produce the largest thrust at a given *St*. The optimum flexibility was observed to shift toward stiffer airfoil structure with increasing *St*. No results are reported in Heathcote and Gursul (2007) regarding the influence of airfoil flexibility on the frequency at which the von Kármán street switches from the traditional to the reverse configuration, as done in the present work.

The Strouhal number used in plotting the data in Fig. 16 is based on the peak-to-peak TE deflection of a rigid airfoil (h_p). For flexible airfoils, the actual TE deflection ($h_{p,actual}$) will generally be different from h_p. Hence, it seems that a Strouhal number based on the actual TE deflection, St_{te}, would be more appropriate in characterizing *b* as well as other parameters of the wake vortex pattern. To examine

this idea, the PIV data are employed to determine b in a more systematic way than from the flow visualization. For this analysis, the sequence of vorticity fields is first phase ordered based on the measured frequency of oscillation of the airfoil. Focusing on $x/c = 0.5$, two phases of the oscillation cycle are identified where the negative and positive vortex core centers are located at this streamwise location (where the vortex centers are taken to correspond to the minimum and maximum vorticity, respectively, within the oscillation cycle). At these phases, the y locations of the vortex cores are determined and b is computed as y for the positive vortex core center minus the corresponding y for the negative vortex. The uncertainty in determining b is estimated to be equal to the PIV grid spacing of $\pm 0.028c$, or 10 % of the largest b/c value observed. The uncertainty in the determination of St_{te} predominantly comes from the error in the measurement of the trailing edge displacement (see Sect. 2). Figure 17 shows b/c plotted versus St (left plot) and St_{te} (right plot). Inspection of Fig. 18 shows that in fact by plotting b/c versus St_{te}, the results exhibit collapse that is not seen when plotting against St.

4.2 Vortex circulation (Γ_o)

For the experimental data, the vortex circulation is obtained from the integral of vorticity over the area occupied by the vortex when the core center is located at $x/c = 0.5$. Because it is difficult to precisely define the boundary of this area, the integration is done by simply summing all vorticity of a given sign within a streamwise extent of one wavelength centered around $x/c = 0.5$: $0.5 - a/2 < x/c < 0.5 + a/2$ (see below for description of the procedure employed to compute a). The result is multiplied by the area of the PIV interrogation cell to yield the numerical integration of the vorticity (or circulation) via "the method of rectangles." The estimated *rms* uncertainty of the circulation is found through propagation of the sub-pixel error of the PIV measurements (0.11 cm/s). The corresponding circulation uncertainty is less than the plotting symbol size. Figure 18 displays the non-dimensional circulation plotted against the Strouhal number at the lowest reduced frequency ($k = 4.63$). As expected, the circulation increases with increasing St. At a given St, the largest circulation is

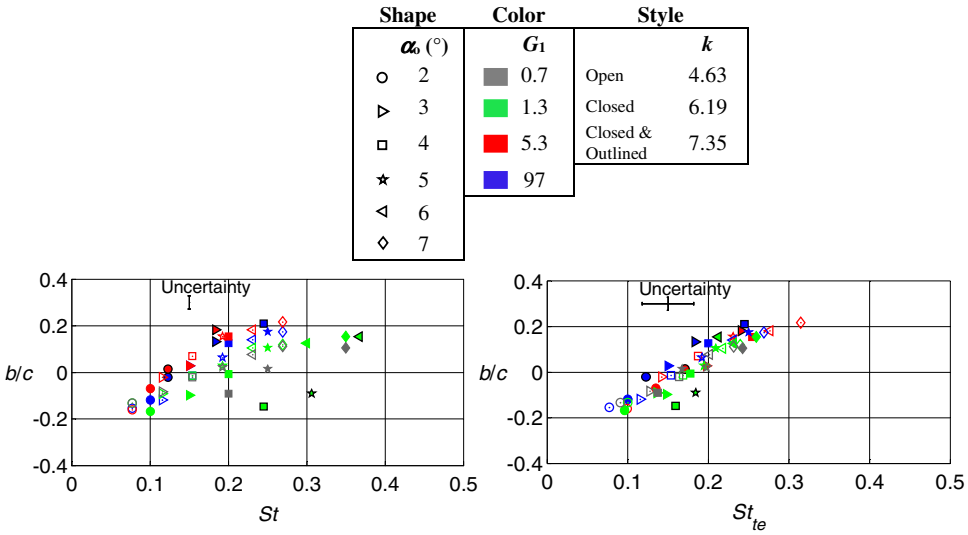

Fig. 17 Dependence of b/c on St (*left*) and St_{te} (*right*); from PIV measurements. The uncertainty in b/c and St_{te} is depicted on the plot

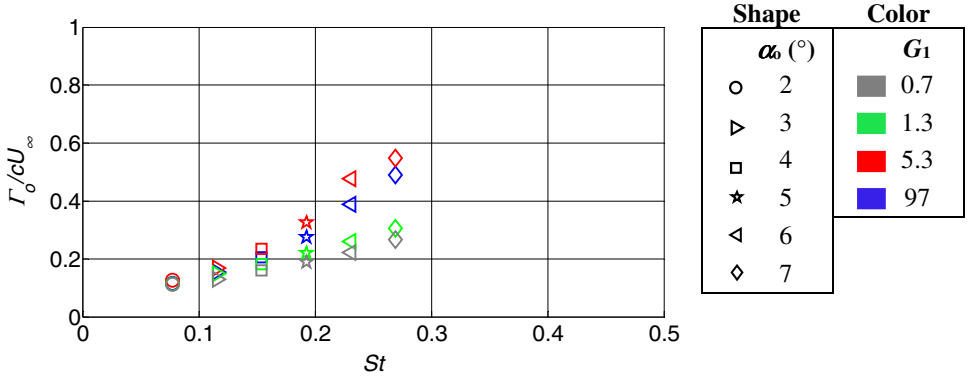

Fig. 18 Variation of Γ_o/cU_∞ with St for $k = 4.63$; from PIV measurements

attained when using the flexible airfoil with the least flexibility ($G_1 = 5.3$; shown using red symbols). The two most flexible airfoils produce the smallest circulation with the difference between the circulations produced by the different airfoils becoming more pronounced as St increases. The qualitative trends seen in Fig. 18 are also found to be similar to those found at the two highest reduced frequencies.

The circulation results for all frequencies are displayed in Fig. 19 when plotted versus St (left plot) and St_{te} (right plot). Similar to b/c results, using St_{te} rather than St as the independent variable gives better correlation of the data; though the data remain more scattered than in the case of b/c.

Since the analysis based on the vortex array model suggests that Γ_o/a is a parameter important to characterizing the mean velocity excess above freestream velocity, the non-dimensional form of circulation Γ_o/aU_∞ is also examined here. The results when using both a and c for normalization of Γ_o are depicted in Fig. 20. It is seen that some improvement in the data collapse (specifically in the case of the rigid and least flexible airfoils; blue and red symbols, respectively) is attained when using a for scaling the circulation; though appreciable scatter still remains.

4.3 Wavelength (a) and convection velocity (U_c)

To compute a, phase-sorted vorticity time series are extracted at a fixed y location and different x locations in the range $0.1 < x/c < 0.9$. The y position is taken to be the same as that of the center of the negative vortex when it is located at $x/c = 0.5$. A cross-spectrum is then computed between the vorticity time series at each of the x locations and that occurring at $x/c = 0.5$. Subsequently, the phase angle of the cross-spectrum at the frequency of oscillation is extracted and plotted versus the streamwise location, as shown in Fig. 21. The linear variation of the phase data

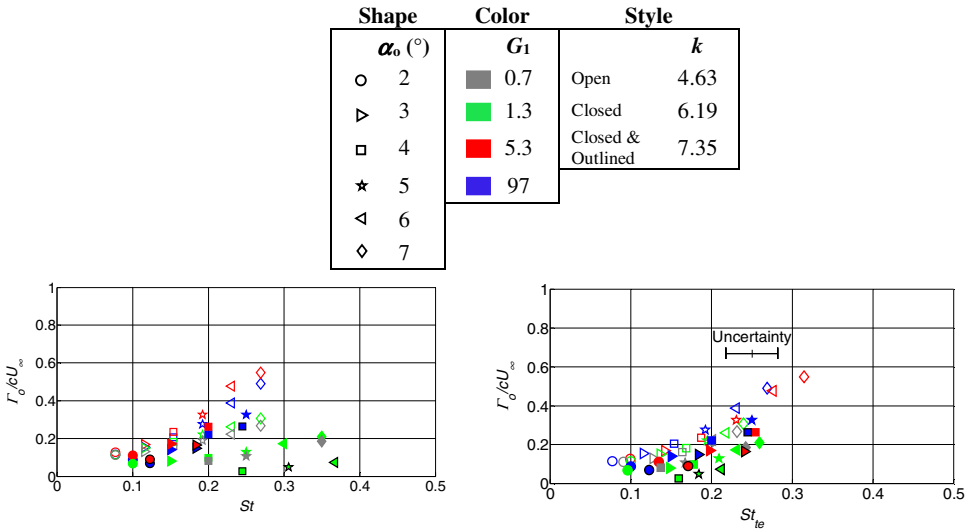

Fig. 19 Variation of Γ_o/cU_∞ with St (*left*) and St_{te} (*right*); from PIV measurements. The uncertainty in St_{te} is depicted on the plot; the uncertainty in Γ_o/cU_∞ is less than the symbol size

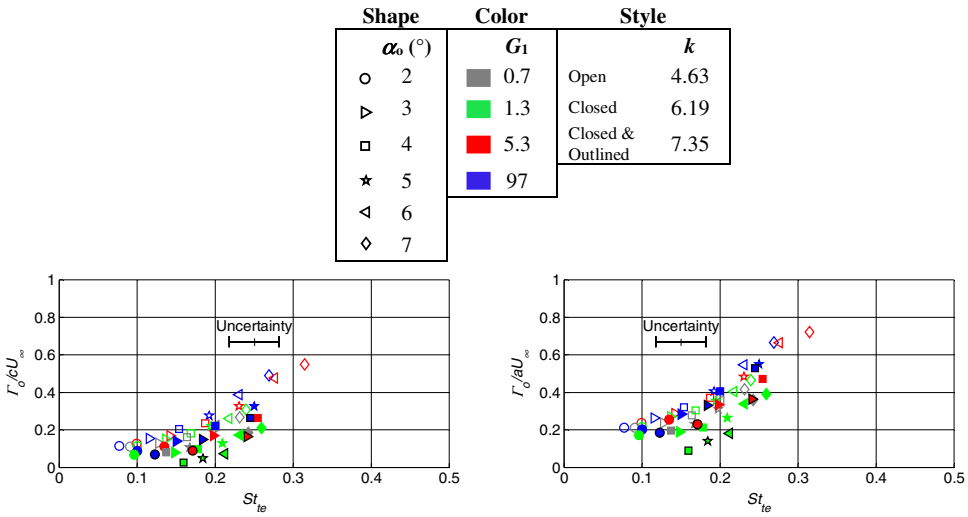

Fig. 20 Variation of Γ_o/cU_∞ (*left*) and Γ_o/aU_∞ (*right*) with St_{te}; from PIV measurements. The uncertainty in St_{te} is depicted on the plot; the uncertainty in Γ_o/cU_∞ and Γ_o/cU_∞ is less than the symbol size

with x is indicative of the traveling-wave-like signature associated with the convection of the vortices. The slope of a linear fit to the data, m, is used to calculate the wavelength: $a/c = 2\pi/m$.

Plots of a/c versus St and St_{te} are shown in Fig. 22 (the uncertainty in a is smaller than the symbol size). Though no overall collapse is found in either plot, when plotted versus St_{te}, the influences of frequency and amplitude on a/c are easy to separate. In particular, in this case, a decent collapse of the data for a given reduced frequency is observed. To facilitate making this observation, a trend line is superposed on the data points representing a given frequency in Fig. 22 (right). The results show that at a given frequency, the wavelength becomes longer with increasing amplitude. On the other hand, the opposite trend takes place with frequency, where a/c decreases with increasing k; e.g., as seen in Bohl and Koochesfahani (2009). This suggests that the data for all three frequencies may collapse well if a is multiplied by the frequency. Such a plot is shown in Fig. 23, where af is normalized by the freestream velocity. It should be noted that af is in fact the convection velocity U_c of the vortex. Accordingly, Fig. 23 is indeed a plot of the convection velocity dependence on St_{te}. As seen from the figure, the data collapse fairly well, exhibiting linear behavior (within the data scatter) with the convection velocity becoming larger with increasing St_{te}. Furthermore, the convection velocity is expected to be the same as the freestream velocity when a neutral wake is established; i.e., when $b/c = 0$ and the mean velocity distribution in

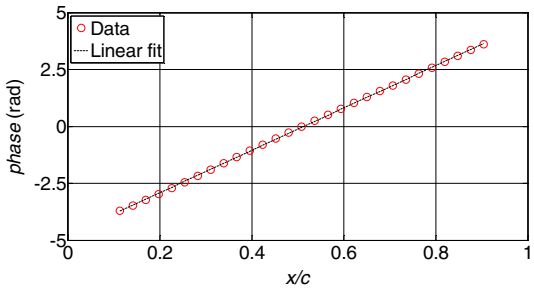

Fig. 21 Example of the variation of the phase angle between the sinusoidal vorticity signature measured at different x/c locations and that measured at $x/c = 0.5$. The data are obtained at y location corresponding to the location of the center of the negative vortex at $x/c = 0.5$

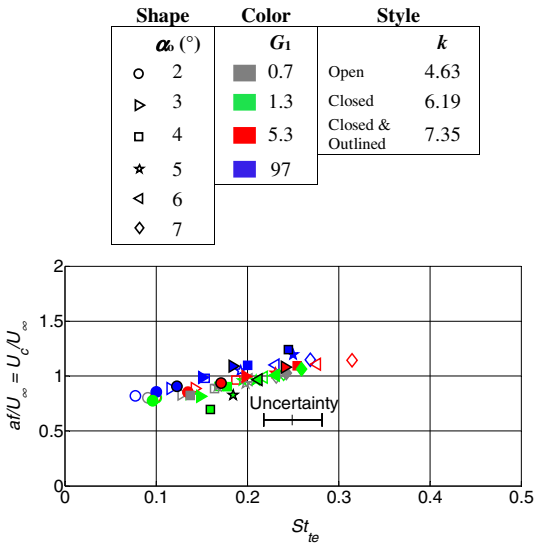

Fig. 23 Dependence of the convection velocity af/U_∞ on St_{te}; from PIV measurements. The uncertainty in St_{te} is depicted on the plot; the uncertainty in af/U_∞ is less than the symbol size. The minimum and maximum of the vertical scale represent 100 % deviation from the approximate average of all data ($U_c/U_\infty = 1$), as is the case in Fig. 22 (*right*), where the average is approximately $af/U_\infty = 0.5$, for fair comparison of data scatter in % between the two plots

Fig. 22 Dependence of a/c on St (*left*) and St_{te} (*right*); from PIV measurements. The uncertainty in St_{te} is depicted on the plot; the uncertainty in a/c is less than the symbol

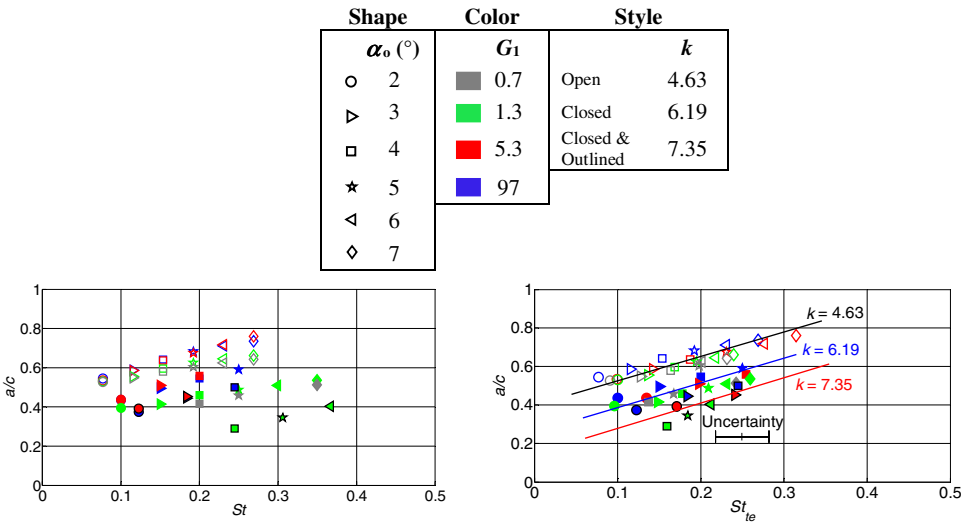

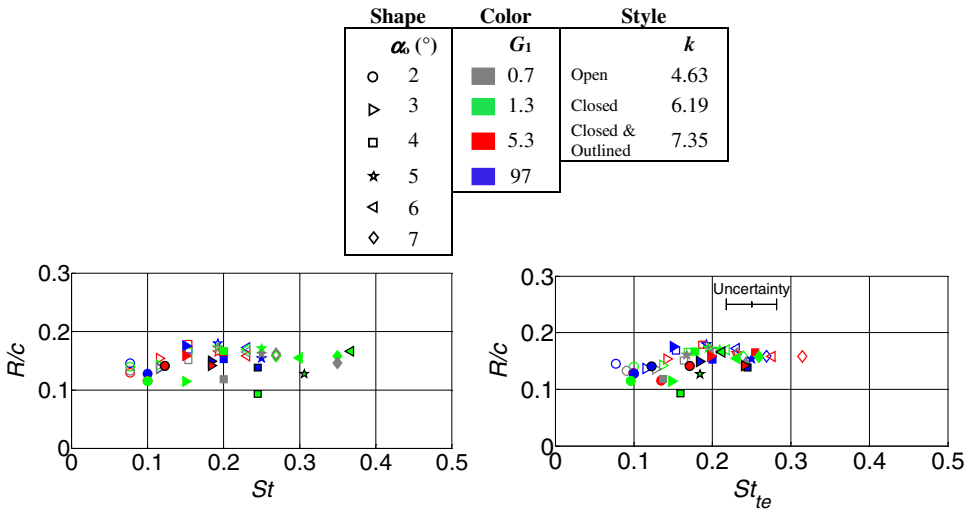

Fig. 24 Variation of R/c with St (*left*) and St_{te} (*right*); from PIV measurements. The uncertainty in St_{te} is depicted on the plot

the wake is uniform and equal to U_∞. Though it is difficult to pinpoint because of data scatter, it appears that U_c/U_∞ assumes a value of 1 in the St_{te} range of approximately 0.15–0.2, which overlaps with the St_{te} range at which $b/c \approx 0$ in Fig. 17.

4.4 Vortex core radius (R)

The vortex core radius is estimated by fitting a Gaussian function of the form:

$$\omega = \omega_o e^{-\frac{(y-y_o)^2}{R^2}} \tag{13}$$

to the measured cross-stream variation of vorticity when the center of a vortex is located at $x/c = 0.5$. In Eq. (13), ω_o is the maximum vorticity at the vortex center, y_o is the y-coordinate of the vortex center, and R is the vortex core radius. The fit is applied for both the positive- and negative-signed vortices, and the value of R is estimated as the average of the two cases. The resulting variation of R with St and St_{te} is shown in Fig. 24. Overall, R/c does not change substantially with Strouhal number while, similar to other vortex characteristics examined earlier, exhibiting better collapse with St_{te} than with St. It is also noteworthy that the R/c values are appreciably higher (by approximately a factor of five) than those reported in Bohl and Koochesfahani (2009) and Naguib et al. (2011). This is believed to be resulting from the lower Reynolds number of the present study: 2010 in comparison with 12,000 in Bohl and Koochesfahani (2009) and Naguib et al. (2011).

5 Thrust coefficient estimation

The information given in Figs. 17 (right), 19 (right), 23 and 24 (right) regarding the variation of the wake vortex parameters with St_{te} is utilized in conjunction with the vortex array model to obtain the mean streamwise force coefficient (C_f) variation with Strouhal number. To do so, a linear fit to the data shown in Fig. 17 (right) and Fig. 23 is used to provide values for b and a, respectively, at different St_{te} values. Since the data collapse is reasonably good in both of these cases, a single fit represents the variation with St_{te} well in each case. On the other hand, the remaining spread in the collapse of the circulation data in Fig. 19 (right) is found to exhibit dependence on the frequency of oscillation of the airfoil. Therefore, in this case, the fit is done for data corresponding to the considered airfoil oscillation frequency. In addition, since the variation of Γ_o/cU_∞ with St_{te} appears nonlinear, a quadratic polynomial rather than a linear fit is used. Also, since R/c does not vary substantially with St_{te}, an average of all measured values is used in the calculation of C_f. The calculation is based on using the model to obtain the phase-resolved u and v information employing Eqs. (2) through (4). Subsequently, the

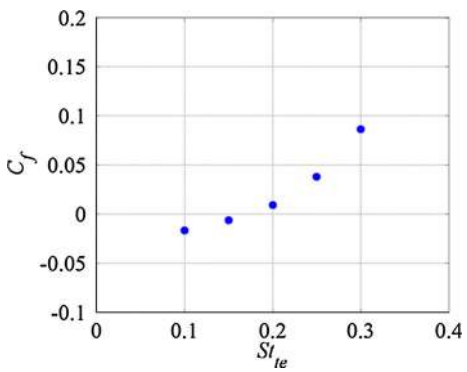

Fig. 25 Variation of C_f with St_{te} at $k = 6.19$ obtained using the vortex array model in conjunction with values of a, b, R and Γ_o obtained using the identified empirical scaling of these quantities, found from the PIV measurements

mean and *rms* velocity profiles are computed and integrated from $y/c = -2$ to 2 according to Eq. (5) to calculate C_f. The selected integration limits are sufficiently far to ensure that U is the same as the freestream velocity and that the *rms* terms have decayed to zero. The accuracy of using the vortex array model to compute C_f has already been demonstrated in Naguib et al. (2011).

Using the procedure explained above and knowing the freestream velocity, frequency of oscillation and chord length, values of a, b, R and Γ_o are obtained at different St_{te} values in the range 0.1–0.3 and used in connection with the vortex array model to compute C_f for $k = 6.19$. The results are shown in Fig. 25. The data exhibit the expected trend of switching from drag ($C_f < 0$) to thrust with increasing St_{te}. It is noted, however, that the accuracy of the C_f results is dependent on the accuracy of the wake vortex parameters, which exhibit a fair amount of scatter, particularly for Γ_o and R (Figs. 19 (right) and 24, respectively). Overall, Fig. 25 highlights the usefulness of coupling empirical scaling of the wake vortex parameters with the vortex array model to estimate the mean streamwise force acting on the airfoil.

6 Conclusions

Particle image velocimetry measurements are taken in the wake of harmonically pitching airfoils possessing a flexible "tail," the structural flexibility of which is varied over three orders of magnitude. Data are obtained at $Re_c = 2010$ for different oscillation amplitudes and frequencies. The focus of the data analysis is on extracting the circulation (Γ_o), the streamwise and cross-stream spacing (a and b, respectively) of the vortices shed into the wake, and the vortex core radius (R). The influence of the airfoil flexibility on how these parameters vary with change in the amplitude and frequency of oscillation is investigated.

The results show that, for a given oscillation amplitude, flexible airfoils require lower reduced frequency of oscillation than their rigid counterpart to exhibit a switch in the wake vortex pattern from classical to reverse von Kármán street (i.e., b switching sign from negative to positive). At a given reduced frequency, an optimum airfoil flexibility exists which results in the earliest switch in the vortex pattern with increasing oscillation amplitude. This optimum flexibility shifts toward stiffer tails with increasing reduced frequency. More interestingly, reasonable correlation for all airfoils examined is found for the variation of b/c with Strouhal number (St) if the latter is defined using the *actual* oscillation amplitude of the trailing edge (St_{te}). Similar correlations are also found for the dependence of the circulation, streamwise spacing, convection velocity and vortex core radius. Additional investigations are required to examine how the identified scaling depends on Reynolds number and airfoil shape.

Using a vortex array model of the wake, insight is gained into the ramification of the observed variation of the wake parameters with St_{te} on the mean thrust acting on the airfoil for the reverse von Kármán wake. The results show that the mean thrust is directly proportional to b but inversely proportional to a. At sufficiently large values of b (which depend on the vortex core radius), the wake vortex pattern may be approximated by two vortex sheets, leading to linear dependence of the thrust coefficient on b. On the other hand, though typically the mean thrust increases with increasing Γ_o, at sufficiently large values of a, the behavior could be non-monotonic, leading to the possibility of producing a net drag force at high values of circulation.

Overall, the combination of the scaling of the wake vortex parameters with St_{te} and the vortex array model provides a useful tool for computation of the net thrust acting on harmonically pitching airfoils. This utility is demonstrated here by using the empirically identified scaling of the wake vortex parameters in conjunction with the vortex array model to estimate the mean streamwise force coefficient variation with Strouhal number. In addition, the understanding of the implications of the wake vortex configuration on the net thrust acting on the airfoil provides basis for an interesting approach for thrust manipulation by attempting to alter the wake vortex pattern to one with desired thrust characteristics.

Acknowledgments This work was supported by AFOSR Grant Number FA9550-10-1-0342; program manager Dr. Douglas Smith.

References

Anderson JM, Streitlien K, Barrett DS, Triantafyllou MS (1998) Oscillating foils of high propulsive efficiency. J Fluid Mech 360:41–72

Bohl DG, Koochesfahani MM (2009) MTV measurement of the vortical field in the wake of an airfoil oscillating at high reduced frequency. J Fluid Mech 620:63–88

Heathcote S, Gursul I (2007) Flexible flapping airfoil propulsion at low Reynolds numbers. AIAA J 45(5):1066–1079

Kang C-K, Aono H, Cesnik CES, Shyy W (2011) Effects of flexibility on the aerodynamic performance of flapping wings. J Fluid Mech 689:31, 32–74

Koochesfahani MM (1989) Vortical patterns in the wake of an oscillating airfoil. AIAA J 27(9):1200–1205

Lai JCS, Platzer MF (1999) Jet characteristics of a plunging airfoil. AIAA J 37(12):1529–1537

Lissaman PBS (1983) Low-Reynolds-number airfoils. Annu Rev Fluid Mech 15:223–239

Lai A, Liu, F (2009) Computation of a rigid airfoil in plunging motion with a flexible trailing beam. AIAA paper 2009-726-685

Mueller TJ, DeLaurier JD (2003) Aerodynamics of small vehicles. Annu Rev Fluid Mech 35:89–111

Naguib AM, Vitek J, Koochesfahani MM (2011) Finite-core vortex array model of the wake of a periodically pitching airfoil. AIAA J 49(7):1542–1550

Ol MV (2007) Vortical structures in high frequency pitch and plunge at low Reynolds number. AIAA paper 2007-4233

Raffel M, Willert CE, Wereley ST, Kompenhaus J (2007) Particle image velocimetry—a practical guide, 2nd edn. Springer, New York

Shyy W, Lian Y, Tang J, Liu H, Trizila P, Stanford B, Bernal L, Cesnik C, Friedmann P, Ifju P (2008) Computational aerodynamics of low Reynolds number plunging, pitching and flexible wings for MAV applications. AIAA paper 2008-523

Thiria B, Godoy-Diana R (2010) How wing compliance drives the efficiency of self-propelled flapping flyers. Phys Rev E 82:015303(R)

Von Kármán T, Burgers JM (1943) General aerodynamic theory—perfect fluids. In: Durand WF (ed) Aerodynamic theory, Division E, vol 2. Springer, Berlin, p 308

Young J, Lai JCS (2004) Oscillation frequency and amplitude effects on the wake of a plunging airfoil. AIAA J 42(10):2042–2052